ACS APPLIED MATERIALS & INTERFACES

Research Article

www.acsami.org

Palladium–Silver Mesowires for the Extended Detection of H_2

Claire Fournier, Khalil Rajoua, Marie-Liesse Doublet, and Frédéric Favier*

Institut Charles Gerhardt, UMR 5253 CNRS – Université Montpellier 2, Place Eugène Bataillon, 34095 Montpellier, France

Supporting Information

ABSTRACT: Palladium–silver mesowires are prepared by electrochemical decoration of graphite step-edges with a good control of the alloy composition and wire diameter. As-prepared arrays are used for hydrogen sensing and demonstrate extended detection capabilities up to the whole concentration range of H_2 depending on the alloy composition. At low silver content, low hydrogen concentration is detected but the sensing window is narrow because of sensor saturation. The sensing window is advantageously extended to higher hydrogen concentrations for quantitative measurements up to pure H_2 flows with Ag-rich alloys. The mechanism responsible for these behaviors implies the statistical distribution in surface composition rather than the structural characteristics and stability domains of the corresponding hydride phases.

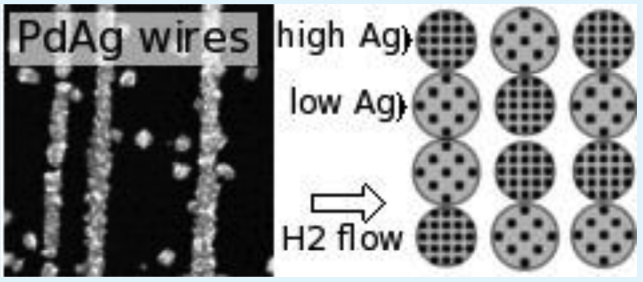

KEYWORDS: *electrodeposition, HOPG, sensing mechanism, in situ XRD, DFT, surface composition*

INTRODUCTION

The potential generalized use of H_2 as fuel for hydrogen powered vehicles and static power generators faces safety issues associated with industrial generation, storage, routing, handling, and mobile or on-site use of this explosive gas.[1] The anticipated demand for fast and reliable H_2 safety sensors has recently induced intensive research and development efforts[2] stigmatized by the tremendous increase of publications (+430%)[3] and patents (+286%)[4] in the field, from 2000 to 2011. It is generally admitted that the targeted detection range of such safety sensors is set to 10–100% of the lowest explosion limit, or LEL. This limit corresponds to 4 vol% H_2 in air, as determined by the NASA. Below this 4 vol% limit, H_2 noise generated by storage and fuel-cell equipments disrupts the safety procedures, thus inducing false positive alarms. At the upper limit, any detection above 4 vol% H_2 in air is obviously useless or too belated. The vast majority of these safety sensors includes palladium in the composition of the sensing part. This comes from the highly selective and reversible formation of palladium hydrides when Pd is exposed to H_2 even at room or moderate temperatures and ambiant pressure.[5] The detection is based on the variation in the physicochemical characteristics of the Pd-based sensing material (mass, volume, refraction index, work function ... and more often electrical conductivity) induced by the hydride formation.[6−17]

Apart from the safety concern, today's demands also lie in H_2 sensors dedicated to other technological uses including leak detection in high-quality welding manufacturing or in a real-time quantitative analysis of hydrogenated mixtures in gas flows arising from hydrogen generation and purification processes, or from industrial dehydrogenation of organic molecules. To the best of our knowledge, no portable H_2 sensor exists for operation in the full detection range from a few parts per million in air to 100% H_2. H_2 detection at parts per million levels or less is usually achieved by highly sensitive tin-oxide-based sensors.[18] Selectivity, response time, and resistance to poisoning are not considered as critical parameters for the specific use in leak detection. Only sensitivity matters. In normal operation mode, the upper detection limit is then a few hundred parts per million because of sensor saturation. It can be extended to a few thousand parts per million, but then response times reach unacceptable limits for use in safety devices. The detection of high H_2 concentrations is also a non trivial challenge since safety sensors usually saturate at 10%H_2 in air or so. Detection is for sure still possible, but not in a quantitative way. In contrast, at high concentration of H_2 in the surrounding atmosphere, response times can be pretty short, which fits well with sensor requirements for real-time monitoring of gas flow mixtures, for example. Detection range can be expanded by sensor design: Zeng et al. have reported the use of bilayers of sputtered Cr/Pd on top of nanostructured filtration membranes for the detection of up to 100% concentration of H_2 in air thanks to material confinement.[19] Xie et al. reported a hydrogen sensor based on coverage controlled films of Pd particles and able to detect in a full concentration range of H_2 with a lowest detection limit lower than 0.5%.[20] Using a different approach, we have recently reported a full concentration range H_2 sensor built on isolated palladium islands ordered in 2D arrays. For this sensor, we have shown that the Pd dot surface roughness and, correlatively, the gap size distribution are responsible for the extended sensing capabilities.[21] Another way to expand the detection range of

Received: September 27, 2012
Accepted: December 4, 2012
Published: December 4, 2012

Pd-based H_2 sensors is certainly to increase the solubility of H_2 in the sensing material. Since the first report by Graham in the second half of XIXth century,[22] it has been suggested that a higher solubility of H_2 can be achieved by alloying Pd with other metals such as Ag, Cu, or Au.[23] More recent works have completed the description of the impact of such alloying in showing (i) an enhancement of the mechanical properties preventing from material embrittlement,[5] (ii) an increase in the H_2 permeability by reducing hydrogen diffusion within the material, as well as (iii) an improvement in the chemical resistance to poisoning.[24−26] Moreover, recent computational studies have corroborated some of these experimental results by providing an advanced description of the electronic structures of these alloys and corresponding hydrides. Lattice parameters and absorption energies of various Pd-based alloys have been computed within the density functional theory (DFT) framework for a better prediction of the solubility properties of H_2 in PdAg and PdAu alloys.[24] In 2001, we have reported the first fabrication of H_2 sensors based on Pd mesowires and obtained by electrochemical step-edge decoration on Highly Oriented Pyrolytic Graphite (HOPG).[27,28] Performances were attractive: high selectivity, fast response, room-temperature operation, diminutive power requirements to less than 100 nW, and good resistance to poisoning by reactive gases, including O_2, CO, and CH_4. Moreover, the response signal was fully proportional from 0.5% to 10% H_2 in air, a concentration range that is perfectly suited for safety purpose. The main goal of the present work is to expand the detection range of such mesowire-based sensors to H_2 concentrations above 10%. In the following, we present the electrochemical method for the preparation of mesowires with various Ag/Pd ratios. After a transfer onto a PVC support, these sensors were hooked to a potentiostat and device characteristics were evaluated in the full concentration range from 0.5% to 100% H_2 in air. Sensing mechanism and performances are here discussed on the basis of the structural information obtained from X-ray diffractions in hydrogenated controlled atmospheres using a simple percolation model.

EXPERIMENTAL SECTION

Electrochemical Measurements and Synthesis. Four different solutions were prepared with various ratios of Ag/Pd: 2/5, 1/5, 1/10, and 1/20. The components were mixed in the following order: $AgNO_3$ (Acros 99.85%), $NaNO_3$, HCl (Fluka 37% traceselect), NaCl (Aldrich 99.99%), and $PdCl_2$ (Alfa Aesar 99.999%). The composition of the plating solutions is listed in Table 1. All electrodeposition experiments were carried out in a one compartment three electrodes cell: An Ag/AgCl electrode was used as reference and a Pt foil was used as counter electrode. The working electrode consists in highly oriented pyrolytic graphite (HOPG) which was freshly cleaved prior to be used and held with a Teflon electrode holder. A PAR12 Autolab potentiostat/galvanostat was operated in potentiostatic mode for the nanowire electrochemical deposition. Nanowires were obtained by electrochemical step-edge decoration on the HOPG surface. This method consists in applying three consecutive potentiostatic pulses: (i) an oxidant potential (+0.8 V) for 5s to chemically differentiate the step edges from the terraces, (ii) a nucleation potential (−0.7 V) for 10 ms, and (iii) a growth potential (solution dependent) for 300s.[29] All potential values given in the following referred to Ag/AgCl. Various growth potentials were tested for each plating solution: for solution 1 the potential varied from −0.1 to 0.23 V, for solution 2 from −0.47 to 0.05 V, for solution 3 from −0.154 to 0.20 V, for solution 4 from 0 to 0.25 V, and for solution 5 from −0.25 to 0 V. Solution 5 is the Pd-only plating solution with the following composition: 0.05 M $NaNO_3$, 2 M NaCl, 0.05 M HCl, and 2 mM $PdCl_2$. After deposition, electrode surfaces were rinsed with water.

Table 1. Compositions of the Various PdAg Plating Solutions Used during the Present Work

	[$AgNO_3$] (mM)	[$NaNO_3$] (M)	[HCl] (M)	[NaCl] (M)	[$PdCl_2$] (mM)
solution 1	1	0.05	0.05	2	2.5
solution 2	0.5	0.05	0.05	2	2.5
solution 3	0.5	0.05	0.05	2	5
solution 4	0.5	0.05	0.05	2	10

Microscopy. Wire arrays as grown at HOPG surface were imaged by scanning electron microscopy (SEM, JEOL 1200 EXII operated at 15 KeV). Sampling was done using aluminum SEM stub and adhesive carbon tape. To get further information on the chemical composition of the electrodeposited PdAg wires, we performed EDX analyses using the same equipment and sampling. Errors on compositions are 1×10^{-4} mol %.

Sensor Fabrication. The sensors were fabricated by transferring the wire arrays from the HOPG surface to a polyvinyl chloride (PVC) surface. PVC was rinsed off with dry ethanol before transfer. The transfer was made using a drop of cyanoacrylate glue. After adhesive hardening, the graphite was lifted off the cyanoacrylate. Using this procedure, a large majority of the initially deposited mesowires were transferred onto the cyanoacrylate surface. Contacts with a 150 μm span were obtained by sputtering platinum through a metal shadow-mask placed at the appropriate surface location with the aid of an optical microscope. Using a silver paste (Acheson-Electrodag, Agar Scientific), some macroscopic copper wires were further attached to these contacts to allow resistance measurements. Following this fabrication procedure, the success rate for operating sensors was about 80%.

Hydrogen Sensing. The as-fabricated sensors were tested on a specially designed test line allowing the generation of controlled flows of either hydrogenated gas mixtures in the concentration range from 0.1 to 100% of H_2 in N_2 or synthetic air used as carrying gas. Two sets of mass-flow controllers were used for high and low H_2/N_2 concentration ranges: 300 mL/min for N_2 and 20 mL/min for H_2 in the 100% to 5% range, and 300 mL/min for N_2 and 3 mL/min for H_2 in the 5% to 0.1% range. At the specific 5% H_2/N_2 concentration, the sensing test is systematically repeated for accuracy control when switching from high to low concentration operating modes. Sensing tests were performed in a Plexiglas flow cell equipped with gas in- and outlets, and cables connectors for electrical measurements. Electrical measurements were performed using the same potentiostat as for the nanowire deposition. Unless otherwise notified, a 20 mV potential bias was applied in between the metal contacts while the corresponding current passing through the nanowire sensitive part was recorded. Sampling time was 1 s.

In situ X-ray Diffraction. In situ X-ray diffraction patterns were collected on an X'pert Philips diffractometer (CuKα). Thick deposits on HOPG were sampled in an Anton Paar gas chamber (HTK1200) connected to our gas-mixture line, operated in the same conditions as for sensing tests. X-ray diffraction patterns were recorded in the $38° < 2\theta < 41°$ range which corresponds to the (111) diffraction peak of $Pd_{100-x}Ag_x$.[30] For calibration purpose, the (100) diffraction peak of the HOPG substrate at 26.35° 2θ was recorded as well. Samples were equilibrated for 5 min under H_2/N_2 flows at chosen concentrations before measurements. Diffraction data were recorded under constant flows at 25 mL/min of H_2/N_2 mixtures for 0, 1, 2, 5 10, 20, 30, and 40 vol % H_2 in N_2.

RESULTS AND DISCUSSION

Synthesis of Palladium−Silver Mesowires. Palladium−silver mesowires were prepared using the same experimental procedure as we have developed for the fabrication of pure Pd mesowire-based H_2 sensors. These mesowires were nucleated and grown at the HOPG step edges which dictate the length

and shape of the final mesowires. The HOPG employed for this study is a polycrystalline material made of grains oriented in the same crystallographic direction (normal to 0001 direction). The predominant defects at HOPG grain surface are incomplete graphite layers that form more or less linear and parallel "step edges" with heights varying from a few angstroms to hundreds of angstroms. The present method consists in a selective electrochemical decoration of these step edges with metal (e.g., Pd or $Pd_{100-x}Ag_x$ alloys). A three-pulse potentiostatic program is applied: an oxidant potential for a few seconds to oxidize the step edges and favor interactions with solvated metal species, a nucleation potential for a few milliseconds and a low overpotential for a few hundreds of seconds to allow the growth of the wires under kinetic control.

Mainly two different plating solutions were used for the electrochemical-deposition of PdAg alloys. Yu et al. have used nitrate Pd^{2+} and Ag^+ salts in sodium nitrate electrolyte for the single pulse deposition of PdAg nanowires.[31] The solubilization of $Pd(NO_3)_2$ is, however, difficult to achieve in nitrate aqueous solutions, and the resulting solutions are rather unstable. In contrast to this chloride-free approach, Monty et al. have electrochemically prepared PdAg nanowires from stable Ag^+/Pd^{2+} mixtures in 2 M NaCl-based electrolytes.[32] In such highly concentrated chlorine solutions, the chemical equilibrium is strongly displaced toward the formation of $Na_nAg_mCl_{m+n}$ soluble species.[33]

For nanowire growth, the applied potentials were extracted from cyclic voltammograms (CV) measurements in plating solutions made of Ag^+ and Pd^{2+} cation mixtures in the NaCl electrolyte. Figure 1 shows the cyclic voltammograms at a

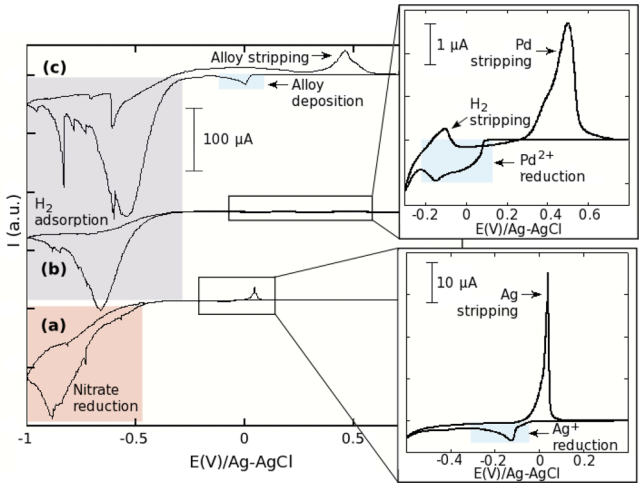

Figure 1. Cyclic voltammograms at a freshly cleaved HOPG surface for solutions containing aqueous 0.05 M $NaNO_3$, 2 M NaCl, 0.05 M HCl, and (a) 0.5 mM [Ag^+], or (b) 2 mM [Pd^{2+}], or (c) 0.5 mM [Ag^+]/2.5 mM [Pd^{2+}] mixture. Highlighted are the areas for metal or alloy depositions (light blue), nitrate reduction (pink), and hydrogen adsorption (light purple).

freshly cleaved HOPG surface for solutions containing (a) aqueous 0.5 mM Ag^+ in 0.05 M $NaNO_3$, 2 M NaCl, and 0.05 M HCl electrolyte, (b) 2 mM [Pd^{2+}] in the same electrolyte, and (c) 0.5 mM [Ag^+]/2.5 mM [Pd^{2+}] mixture in the same electrolyte. In Figure 1a, the intense reduction wave at −0.8 V vs Ag/AgCl in the silver containing solution corresponds to the catalytic reduction of nitrates at the deposited silver surface.[34,35] As a matter of fact, the reduction of Ag^+ as Ag at the HOPG surface can unambiguously be identified by the small negative current signal measured at about −0.1 V (see the insert of Figure.1a). The positive wave at 0 V in oxidation corresponds to silver stripping from the HOPG surface. Noteworthy that Penner et al. have prepared silver nanowires grown at −0.18 V from 100s to 10000s using the three-step electrochemical procedure described above and in a potential range fully consistent with our measurements (light blue area, Figure 1a).[36]

At first sight, Figure 1b mainly shows a strong negative wave at −0.65 V vs Ag/AgCl corresponding to the adsorption of H_2 at the electrode surface. Signal noise at larger under-potential (lower potentials) arises from the hydrogen evolution. A closer look at the CV in the −0.3 − +0.8 V range (see inset of Figure 1b), however, reveals a small reduction wave with a maximum intensity at −0.1 V vs Ag/AgCl corresponding to the deposition of Pd at the HOPG surface. In contrast, the freshly cleaved and bare HOPG surface neither absorbs H_2 nor reduces water at such potentials: in 0.05 M $NaNO_3$, 2 M NaCl, and 0.05 M HCl electrolyte free of any metal cation, H_2 evolution begins at potential below −0.7 V vs Ag/AgCl, whereas no H_2 adsorption is observed (data not shown). The palladium coating at the HOPG surface thus appears as the only rationale to the H_2 adsorption wave presently observed. Pd stripping arises at potentials higher than 0.3 V vs Ag/AgCl. The Pd wires can be formed by first applying a plating potential of −0.8 V for 5 ms and then growing the resulting Pd nuclei at potentials ranging from −0.3 to −0.5 V (light blue area, inset of Figure 1b). In this potential range, the Pd-deposition occurs predominantly at step edges. Resulting wires are continuous and hundreds of micrometers long.[28]

From CVs measured in palladium-only and silver-only plating solutions, Ag^+/Ag and Pd^{2+}/Pd reduction potentials at the HOPG surface were measured at −0.05 and −0.09 V, respectively. These two reductions occur at nearly equivalent potentials which were further confirmed by running the CV of an Ag^+/Pd^{2+} mixture. For the 1/5 [Ag^+]/[Pd^{2+}] mixture, two negative waves are observed at 0 V and −0.55 V in Figure 1c. The first one corresponds to the simultaneous reduction of Ag^+ and Pd^{2+} cations at the HOPG surface to form the corresponding PdAg alloy. As for measurements done in the Pd-only plating solution (Figure 1b), the second is assigned to the H_2 adsorption. The larger wave intensity and the shift toward less reductive potentials observed from −0.7 V for the Pd-only solution to −0.55 V for the Ag/Pd solution suggests that Ag/Pd alloys are more efficient for H_2 adsorption than pure Pd. On the oxidation side, the complex wave centered at +0.5 V corresponds to the alloy stripping.[37]

Figure 2 shows the cyclic voltammograms measured at a freshly cleaved HOPG surface for solutions containing 0.05 M $NaNO_3$, 2 M NaCl, and 0.05 M HCl electrolyte with aqueous mixtures of (a) 0.5 mM [Ag^+]/10 mM [Pd^{2+}], (b) 0.5 mM [Ag^+]/5 mM [Pd^{2+}], (c) 0.5 mM [Ag^+]/2.5 mM [Pd^{2+}], (d) 1 mM [Ag^+]/2.5 mM [Pd^{2+}]. The whole series shows the same distribution of reduction waves with slight variations in intensity and potential. The negative wave assigned to the Pd/Ag alloy deposition shifts from 0 V to +0.1 V as the palladium content is increased in the plating solutions. The adsorption phenomenon occurring at low-potential is not affected by the composition of the solutions because neither the wave shape nor the wave potential are modified in the whole series. In contrast, the increase in Pd content comes along with

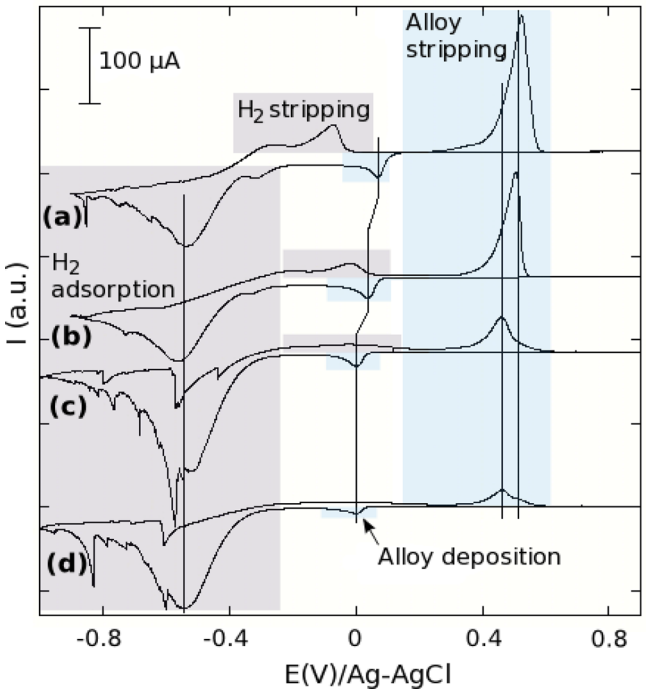

Figure 2. Cyclic voltammograms at a freshly cleaved HOPG surface for solutions containing 0.05 M $NaNO_3$, 2 M NaCl, and 0.05 M HCl electrolyte with aqueous mixtures for (a) 1/20 $[Ag^+]/[Pd^{2+}]$ ratio (0.5 mM $AgNO_3$/10 mM $PdCl_2$), (b) 1/10 $[Ag^+]/[Pd^{2+}]$ ratio (0.5 mM $AgNO_3$/5 mM $PdCl_2$), (c) 1/5 $[Ag^+]/[Pd^{2+}]$ ratio (0.5 mM $AgNO_3$/2.5 mM $PdCl_2$), and (d) 2/5 $[Ag^+]/[Pd^{2+}]$ ratio (1 mM $AgNO_3$/2.5 mM $PdCl_2$).

the appearance of extra positive waves at lower potentials (at about −0.1 V).

These waves correspond to a H_2 stripping occurring at the deposited alloy surface. The presence of Pd thus enhances the reversibility of the adsorption phenomena at the alloy surface. Finally, although metal stripping is observed at 0.05 V for Ag-only and at 0.5 V for Pd-only plating solutions, respectively, complex alloy stripping waves are observed in a large potential range from 0.3 V to 0.6 V. This demonstrates the complexity of PdAg costripping phenomena. The stripping features are characterized by a broad band centered at +0.45 V with two main contributions. Depending on the $[Ag^+]/[Pd^{2+}]$ ratio of the plating solution, the CVs show drastic changes in this potential range, in particular as regards to the relative intensity of the two contributions. As seen above, the overlap of the Pd^{2+} and Ag^+ reduction waves is, at first sight, highly favorable for the simultaneous deposition of these metals and for the formation of PdAg alloys. Using the 1/5 $[Ag^+]/[Pd^{2+}]$ plating solution, after an oxidation pretreatment at +0.8 V and a nucleation pulse at −0.7 V, a long pulse at 0 V results in the growth of long and continuous mesowires. Energy Dispersive X-ray analysis (EDX) of the wires reveals the simultaneous presence of Pd and Ag for the formation of a AgPd alloy with 15 mol %Ag. This approach was generalized using plating solutions of various Pd^{2+} and Ag^+ compositions for the preparation of PdAg mesowires. Table 2 summarizes the silver content in the PdAg deposits (as determined by EDX), the composition of the plating solution and the potential windows used for the mesowire growth.

Interestingly, the final Ag and Pd content of the deposits strongly depends on the relative Ag/Pd composition of the

Table 2. $[AgNO_3]/[PdCl_2]$ Plating Solution Compositions and Corresponding Silver Content (in mol %) Determined by EDX Analysis in PdAg Wires Deposited at Growth Potentials in the Given Potential Window[a]

	$[AgNO_3]/[PdCl_2]$			
	2/5	1/5	1/10	1/20
mol % Ag (EDX)	20(1)	15(1)	10(1)	5(1)
V_{min}/V_{max}	−0.02 V/ +0.17 V	−0.1 V/ 0 V	−0.1 V/ +0.2 V	+0.07 V/ +0.2 V

[a] V_{min}/V_{max} corresponds to the potential window with a constant Ag content.

plating solutions: the higher the $[AgNO_3]/[PdCl_2]$ ratio, the higher the silver content in the resulting PdAg alloys. In a lower extent, the deposition potential also influences the composition of the deposited PdAg structures: the higher the potential, the higher the silver content. Figure 3 shows the characteristic SEM

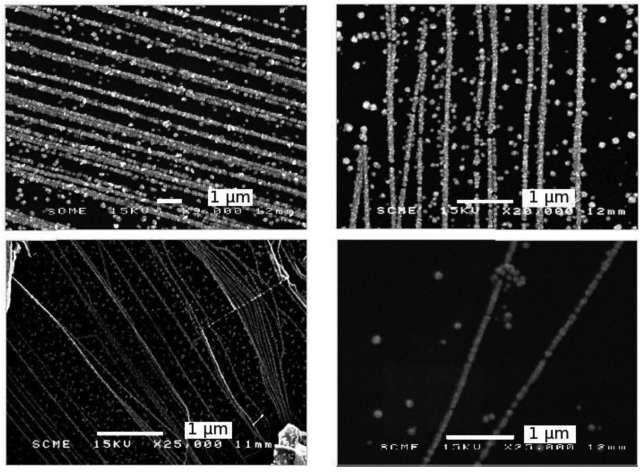

Figure 3. SEM images of PdAg mesowires grown for 300 s (a) from 1/20 $[Ag^+]/[Pd^{2+}]$ solution at 0.13 V, (b) from 1/10 $[Ag^+]/[Pd^{2+}]$ solution at 0.15 V, (c) from 1/5 $[Ag^+]/[Pd^{2+}]$ solution at 0.04 V, and (d) from 2/5 $[Ag^+]/[Pd^{2+}]$ solution at 0 V.

images of the PdAg mesowires electrochemically grown at HOPG surfaces, in a potentiostatic mode and from various plating solutions. Although Tang et al. have recently prepared PdAg nanowires using a single-pulse deposition technique,[38] the three-step preparation method described above allows an optimal control of the mesowires nucleation and growth along the step edges.[39] Of course, this is directly related to the oxidation and nucleation steps preceding the wire growth. As a result, the chemical differentiation of step edges and terraces, and the high density of nuclei (see Figure SI1 in the Supporting Information) along the step edges, afford some flexibility in the overpotential value required for the successful preparation of long and continuous wires. Note that the growth overpotentials have to be adjusted for any given material deposition under kinetic control to limit the simultaneous nucleation/growth of particles on terraces. At selected growth potentials, the resulting wires can be long and continuous, regardless of the plating solution composition or resulting alloy composition. Wire length, shape, and surface density depend on the length, shape, and surface density of the step-edges on which they have grown.

dx.doi.org/10.1021/am302143m | ACS Appl. Mater. Interfaces 2013, 5, 310−318

Given the growth potentials presently used, the mesowire diameter is fully controlled by the electrolysis duration. The corresponding current transients reach a pseudo-steady-state deposition current after a few tens of seconds (see Figure SI2 in the Supporting Information), leading to a simple expression of the wire radius vs the square-root of time:[29]

$$r(t) = \sqrt{\frac{2i_{dep}t_{dep}V_m}{\pi nFl}} \quad (1)$$

with i_{dep}, the steady-state deposition current, V_m the molar volume of the deposited material, n the number of electrons transferred for the deposition of each metal atom, F the Faraday constant, and l the total length of mesowires on the graphite surface.

This linear relationship is depicted in Figure SI3 in the Supporting Information. The data corresponding to short growth durations show excellent fits with simple affine functions in accordance with expression 1. The curve slope is controlled by $(i_{dep})^{1/2}$ and the greater the applied potential, the greater the steady-state deposition current and the larger the corresponding slope. Under this kinetically controlled regime, each individual wire is growing independently on its neighbors. For long duration electrolyzes, wires become large and their measured diameters deviate from eq 1 because of interwire diffusion coupling.[40]

Sensor Performances. Palladium mesowire arrays transferred onto PVC substrates were operated as hydrogen sensors by applying a 20 mV bias and by measuring the corresponding current. The data in panels a and c in Figure 4 show typical sensor signal outputs (plotted here as current transient) when exposed to gas mixtures of various hydrogen contents in nitrogen as carrying gas. Exposure to hydrogenated gas flows induces an increase of the current through the device corresponding to an increase of the conductivity of the mesowires spanning evaporated Pt contacts (see Figure SI4 in the Supporting Information). After a few seconds or a few tens of seconds of exposure, the measured current reaches a plateau corresponding to the maximum conductance of the sensor for a given H_2 concentration. Back to a H_2-free atmosphere, the current drops down and slowly stabilizes after a couple of minutes. During this recovery stage, the sensor was left at open air for a natural regeneration of the cell atmosphere back to air. The sensor can be operated for several H_2/N_2 to air cycles with a remarkable signal repeatability (see Figure SI5 in the Supporting Information). The observed baseline drift, which can be either positive or negative, strongly depends on the way measurement was performed and mainly on the time left for signal recovery. Be what it may, after several H_2/air cycles, the baseline stabilizes without any change in the sensing performance. The signal shape observed during both sensor response and recovery has been described elsewhere for nanogap-based hydrogen sensing devices.[41] It originates from the reversible closing of nanoscopic gaps in discontinuous wires, caused by the dilation of palladium−silver grains undergoing hydrogen absorption. In the absence of hydrogen gas, wires showing closed nanogaps reverted to open circuits.

From Figure 4, it also appears that the amplitude of the signal output is, to some extent, proportional to the hydrogen concentration in the flow the sensor was set. At first sight, the lower the hydrogen content, the lower the current amplitude change. Current changes do not however look linearly proportional to the hydrogen concentration, especially at low

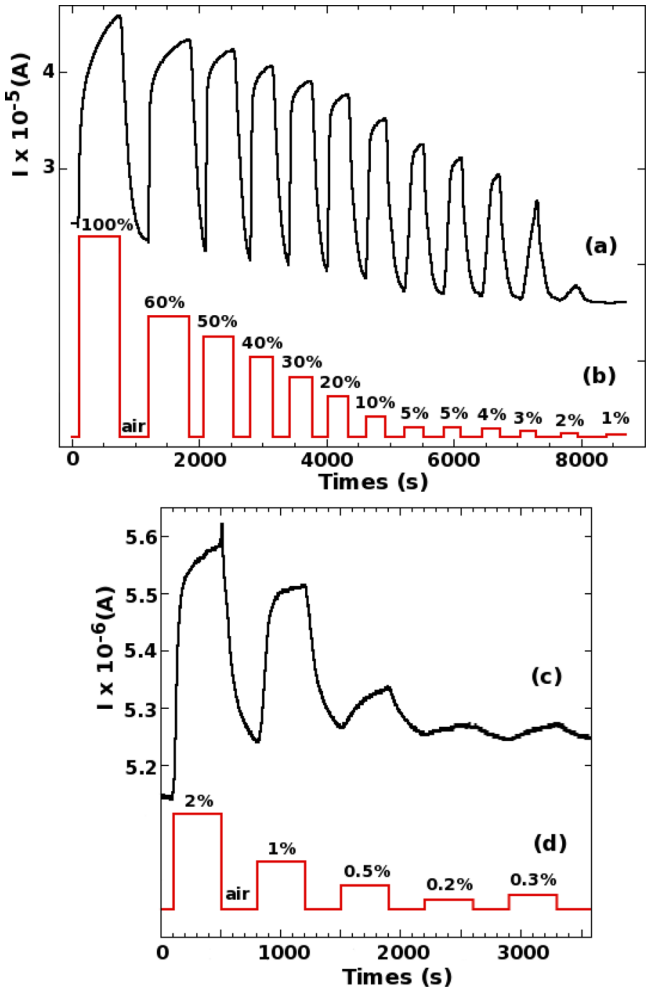

Figure 4. (a) Current response of a $Pd_{85}Ag_{15}$ sensor to hydrogen/nitrogen mixtures and (b) the corresponding H_2 concentrations (in % in N_2). (c) Current response of a $Pd_{95}Ag_5$ sensor to hydrogen/nitrogen mixtures with corresponding concentrations as shown in (d) (H_2 concentration in %, as shown). Data were acquired in random order of H_2 concentration.

concentrations (Figures 4c and 4d) while, at high hydrogen concentration, output signal of the $Pd_{85}Ag_{15}$ sensor seems to saturate above 60% H_2 in N_2 (Figures 4a and 4b). Figure 5 shows the relative current amplitude changes as a function of the hydrogen concentration for various fabricated sensors. Sensing capabilities of PdAg mesowire-based sensors with 0, 5, 10, 15, and 20% Ag in Pd were evaluated. They all detect hydrogen.

The sensors exhibit sigmoid shape of current versus hydrogen concentration response. As depicted in Figure 5, the response shows a sloppy plateau at "low" H_2 concentrations, a quasi-linear hump where the best sensor accuracy is achieved, and a plateau corresponding to the sensor saturation. For each tested sensor, data points in Figure 5 could be fitted using Boltzmann functions which, in agreement with theoretical predictions, confirm the probabilistic nature of the conduction process across the wire arrays.[42] However, the features, in terms of shape and amplitude of these sigmoid curves, strongly depend on the Pd/Ag mesowire composition. For sensors fabricated from pure palladium mesowires, the low concentration plateau is not observed and the output current is fully proportional from 0.1%, as the lowest H_2 concentration tested

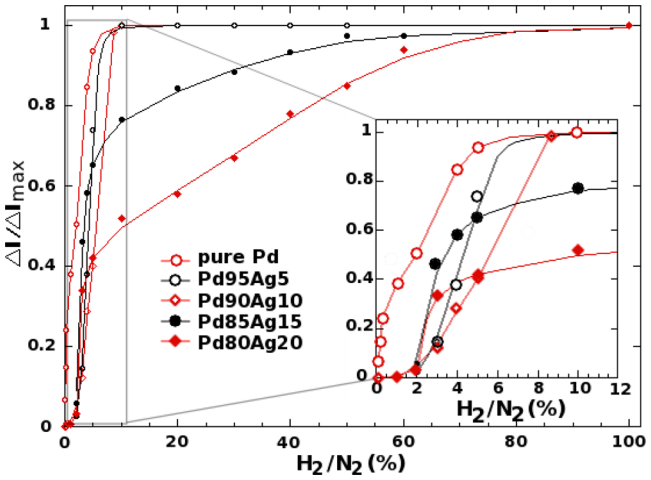

Figure 5. Normalized current amplitudes versus H_2 concentration for the various $Pd_{100-x}Ag_x$ sensors fabricated. Insert shows a zoom-in of the sensor responses for H_2 concentrations below 10% in N_2. Marker sizes are related to errors on measurements.

here, to 6% H_2 in N_2 before sensor saturation at higher hydrogen concentrations. At low silver contents, i.e., $Pd_{95}Ag_5$ and $Pd_{90}Ag_{10}$, the sigmoid curves are still quite sharp. Low concentrations of hydrogen could then be detected, down to 0.2% H_2 in N_2, but the accuracy of the measure below 2% H_2 is rather limited. For both sensors, the best accuracy is achieved between 2 and 8−10% H_2 in N_2 before saturation is reached at higher concentrations. By increasing the silver content, the low concentration plateau disappears since $Pd_{85}Ag_{15}$ and $Pd_{80}Ag_{20}$ sensors are both found insensitive to low hydrogen content atmospheres below 1% H_2 in N_2. The high accuracy step then tends to be limited in the 2 to 5% H_2 range, but is followed by a less steep slope eventually up to the highest H_2 concentrations without any saturation plateau. As such, even if the anticipated accuracy is lower, the signal outputs of these sensors remain proportional up to pure H_2 for extended quantitative sensing capabilities. These results demonstrate that the quantitative hydrogen detection range of the PdAg mesowire-based sensors can be advantageously tuned over the whole hydrogen concentration range by controlling the composition of PdAg alloys. Noteworthy, concentration range sensing capabilities do not depend on the diameter of wires in the arrays. Only the baseline level under air is actually affected: arrays of wires of larger diameters give high conductivity baselines but the relative conductivity changes under hydrogen remain the same, as for thinner wire-based sensors for which the baseline shows a lower conductivity. In the present case, at low silver content, the lowest hydrogen concentrations can be detected but the sensing window is narrow since sensors quickly saturate. Increasing the silver content progressively expands the sensing window to the highest hydrogen concentrations for quantitative measurements up to pure H_2 flows. In contrast, these high silver content sensors are insensitive to low hydrogen concentrations. The mechanism responsible for these behaviors is discussed below.

Sensing Mechanism. As confirmed by SEM imaging (Figure 3), the developed electrochemical method produces wires with similar morphological characteristics including diameter, length and surface roughness, in the whole $Pd_{100-x}Ag_x$ alloy series. Thanks to the design of the evaporated metal contacts through stencils of given span and dimensions, the fabricated sensors statistically include the same number of wires, particles and gaps. Moreover, all particles are quite homogeneous in composition and size. The alloy composition can then be pointed out as the leading parameter for sensing characteristics. The material swelling inducing the gap closing relies on the alloy volume changes associated with the hydride formation, which also depends on the alloy composition. It then makes sense to explore the crystallographic characteristics of the various alloys depending on their composition. Pd and PdAg alloys crystallize in a face centered cubic (fcc) cell. After adsorption at Pd catalytic surface, hydrogen diffuses into the bulk in its dissociated form, H, by hops between available Oh and Td sites. The literature however suggests that in pure palladium, H residency time is much larger in the Oh sites as compared to the Td sites thanks to favorable binding energy.[24] First-principles DFT calculations here performed in a 2 × 2 × 2 supercell confirm this fact by showing that the Td site energy is disfavored over the Oh site energy by no less than 200 meV/H at very low H concentration (see Figure SI6 in the Supporting Information). At low hydrogen concentration (or pressure) in the atmosphere, a α palladium hydride phase is formed without any impact on the pristine crystal cell characteristics (measured at $a_0 = a_\alpha = 3.884(1)$ Å). Increasing H_2 concentration leads to the formation of a β-palladium hydride phase. Although the β-phase remains fcc, the cell parameter experiences a drastic increase up to $a_{\beta max} = 4.027(1)$ Å (measured) corresponding to a 12% cell volume increase. This volume change accounts for the material swelling and gap closing at the origin of the sensing mechanism. Moreover, this maximum volume change of about 12% corresponds to the fully hydrogenated $PdH_{0.7}$ phase, but the β-phase can also be experimentally observed at lower H/Pd ratio for lower volume changes by exposure at some intermediate H_2 concentrations. Evidence for these two latter points is given in Figure 6a where selected d-space ranges of X-ray diffraction patterns are shown for a pure palladium thick deposit corresponding to the (111) diffraction peak measured in situ under pure N_2 and H_2/N_2 flows at 1, 2, 5 10, 20, 30, and 40 vol % H_2 in N_2. This series of patterns shows the evolution of the material crystallographic characteristics upon Pd hydride formation and demonstrates the α to β transition as a biphasic mechanism. At low hydrogen concentration, a single (111) peak is measured at $d_{(111)} = d_0 = 2.243(1)$ Å corresponding to the α-phase. At intermediate H_2 concentrations, a second peak characteristic of the β-phase appears at $d_{\beta min} = 2.319(1)$ Å. As H_2 concentration is increased, the α-phase is progressively converted in the β-phase, as demonstrated by the corresponding peak balance: the d_0 peak intensity keeps on decreasing while the d_β peak increases. Simultaneously, the latter peak shifts to higher distances up to $d_{\beta max} = 2.325(1)$ Å as the hydrogen content increases. This is indicative of simultaneous biphasic and solid solution processes up to the formation of $PdH_{0.7}$, composition generally assumed as characteristic of the fully hydrogenated β-phase.

Alloying palladium with silver induces several changes in the reactivity toward H_2 gas. Based on Monte Carlo simulations, Kurokawa suggested that hydrogen atoms preferentially diffuse by jump through the "palladium-rich regions" of PdAg alloys rather than "silver-rich regions".[43] This is fully consistent with the smaller affinity of hydrogen toward silver compared to palladium to form M−H bonds. On the crystallographic side, the progressive substitution of Pd for Ag in a continuous miscible structure over the whole composition range considered induces an increase in the fcc cell volume that

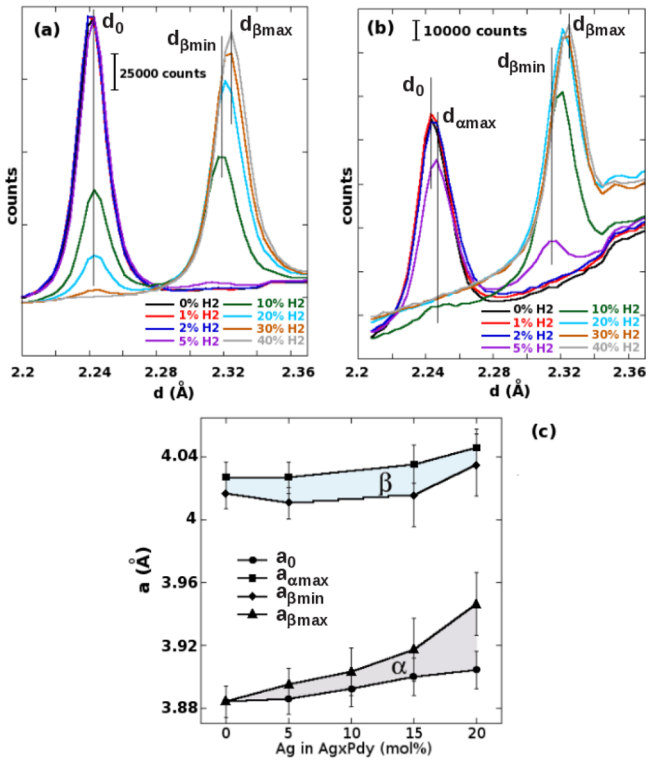

Figure 6. (111) X-ray diffraction peaks of (a) pure Pd and (b) $Pd_{95}Ag_5$ alloy electrodeposited onto HOPG surface measured in situ under various H_2 in N_2 atmospheres. d_0 corresponds to the (111) diffraction peak measured in air, $d_{\alpha max}$ corresponds to the last measurable (111) diffraction peak of the hydride α-phase (i.e., before α-phase disappearance), $d_{\beta min}$ corresponds to the first measurable (111) diffraction peak of the hydride β-phase (ie at β-phase appearance), and $d_{\beta max}$ corresponds to the (111) diffraction peak of the fully hydrogenated β-phase. (c) Evolution of the characteristic cell parameters calculated from the corresponding $d_{(111)}$ as a function of the silver content in $Pd_{100-x}Ag_x$ electrodeposited alloy.

follows a Vegard law. This larger cell volume accounts for the larger atomic/covalent radii of Ag (160 pm) compared to Pd (137 pm). First-principles DFT calculations show that the presence of silver in these expanded cells disrupts the binding energy balance between Oh and Td sites because of unfavorable Ag−H interactions.[24] Several crystallographic differences can also be experimentally observed by comparing the in situ X-ray diffraction patterns corresponding to the various alloys under hydrogenated atmospheres.

Figure 6b shows the (111) diffraction peak intensity and position changes of $Pd_{95}Ag_5$ alloy deposit depending on the H_2 concentration in the gas chamber. As for pure Pd, hydride formation proceeds by a α- to β-phase transition with a progressive decrease of the α peak intensity to the benefit of the β peak, as hydrogen concentration is increased. The main difference with pure Pd is a shift of the α peak from $d_{(111)} = d_0 = 2.242(1)$ Å to $d_{\alpha max} = 2.247(1)$ Å (measured at the disappearance of the peak), whereas the shift in the β peak from $d_{\beta min}$ to $d_{\beta max}$ remains about 0.01 Å. A solid solution domain then appears in the α-phase which was not observed for pure Pd mesowires. Similar in situ experiments were repeated for deposits of $Pd_{90}Ag_{10}$, $Pd_{85}Ag_{15}$, and $Pd_{80}Ag_{20}$ (see Figure SI7 in the Supporting Information). For clarity purpose, the measured distances were converted into $a_{\alpha max}$, $a_{\beta min}$ and $a_{\beta max}$ cubic cell parameters. These parameters are reported in Figure 6c for the whole series of prepared $Pd_{100-x}Ag_x$ wires. A similar increase of the cell parameters is observed for both $Pd_{100-x}Ag_x$ alloys (a_0 as solid circle data) and the corresponding fully converted hydrides ($a_{\beta max}$ as solid square data) as the silver content increases from 0 to 20%. The shift from a_0 to $a_{\beta max}$ corresponds to the maximum material swelling upon hydrogenation. However, because it remains constant in the alloy series, it cannot be considered as responsible for the distinct signal proportionality behaviors observed for the various fabricated sensors. Whatever the alloy composition in the series from pure Pd to $Pd_{80}Ag_{20}$, the shift from $a_{\beta min}$ (solid diamond) to $a_{\beta max}$ remains roughly unchanged as well (light blue area). In contrast, the α peak shift from a_0 to $a_{\alpha max}$ (solid triangle) progressively increases with the silver content (light gray area). This latter shift corresponds to the so-called miscibility gap decrease/disappearance between α and β phases as silver content increases.[44,45]

Either for pure Pd or $Pd_{100-x}Ag_x$ alloys, it is tempting to assign the observed peak shifts to the proportionality of the sensor response because the number of closed gaps (and therefore the number of continuous wires) progressively increases in the array as the material volume increases. Moreover, the enlarged solid solution domain of the α-phase could also be pointed out to explain the extended sensibility (proportionality) performances of $Pd_{100-x}Ag_x$ compared to pure Pd where only β peak shifts. But it is not, from either pure volumic or extra site occupation considerations. In pure Pd, from β_{min} ($d_{\beta min}$) to β_{max} ($d_{\beta max}$), the volume increase experimentally measured, is less than 1% (0.8%). In $Pd_{80}Ag_{20}$, which corresponds to the largest sensibility window, the volume increase from β_{min} to β_{max} is about the same (0.9%), whereas from α_{min} (d_0) to α_{max} ($d_{\alpha max}$) it is limited to at most 3%. These variations are too small with respect to the overall 12% volume increase from pure $Pd_{100-x}Ag_x$ (d_0) to the corresponding fully hydrogenated phase ($d_{\beta max}$).

On the other hand, the linear volume increase with silver content could explain the enlarged solid solution domain of the α-phase through the opening of Td-sites for H insertion in the fcc $Pd_{100-x}Ag_x$ bulk. Once again it is not. The Vegard law experimentally observed for the $Pd_{100-x}Ag_x$ alloys unit cell parameter is very well reproduced by our supercell DFT calculations (with relative errors with experiments less than 1%) in the whole silver content range from 0 to 50 molar %, though this volume increase with the silver content is not sufficient to open Td site even at low hydrogen content (H = 1/32). As shown in Figure SI8 in the Supporting Information, regardless of the silver content, the Pd/Ag−H(Td) distance in the low hydrogenated $Pd_{100-x}Ag_x$ alloys remains significantly lower than the Pd−H(Oh) distance in the low hydrogenated Pd α-phase, therefore leading to unfavorable Td site energies (see Figure SI6 in the Supporting Information).

As explained above, the formation of palladium hydride is a biphasic process involving a progressive conversion of a hydrogen-poor/small cell volume hydride (α-phase) in a hydrogen-rich/large cell volume β-phase. Increasing the H_2 pressure (or H_2/N_2 concentration) leads to a linear increase of the palladium grain average volume as α-phase domains are progressively converted into β-phase domains up to the complete conversion of the whole grain in β-phase hydride. Because volume expansions remain in the whole $Pd_{100-x}Ag_x$ series, the extended sensing performances observed for alloys with increasing silver content do not have crystallographic origins. Alloying Pd with Ag is also known to impact the

elasticity characteristics of the corresponding material:[5,46] the bulk modulus decreases with the silver content in $Pd_{100-x}Ag_x$ alloys as confirmed by DFT calculations. However, the ease of grain deformation under hydride formation in alloys is expected to expand the detection window toward the low H_2 concentrations but not toward the high concentrations.

A possible explanation lies in the probabilistic nature of the sensing mechanism. The amplitude of the detection signal depends on the number of wires made continuous at a given H_2 concentration. Since a continuous wire implies the closing of all gaps between grains, the signal amplitude depends on the probability of closing all gaps in any given wire. This probability follows a Boltzmann distribution law confirming the electronic transport as driven by a percolation process.[42] For pure palladium-based sensors, the grains are statistically close in terms of chemical composition, size, and morphological characteristics and the wires should tend to switch on (respectively off) in a narrow H_2 concentration range: the Boltzmann distribution law is narrow and so is the corresponding $I = f([H_2]/[N_2])$ sigmoid.[27,28] The second consequence of alloying silver with palladium is on the H_2 adsorption properties: the higher the silver content, the lower the number of Pd catalytic sites available at the wire surface for H_2 dissociative adsorption, and the higher the H_2 concentration (pressure) needed for hydride formation. Consequently and as confirmed experimentally (see previous section), higher silver contents lead to limited sensing capabilities at low hydrogen concentrations. On the other hand, silver and palladium atoms are statistically distributed at the grain surface meaning that some grains exhibit Pd-rich surfaces, whereas others present Ag-rich surfaces (although the overall composition of the deposit corresponds to a given Ag/Pd ratio). This surface composition distribution leads to discrepancies in the H_2 adsorption from one grain to another and consequently various H_2 pressures required for hydride formation from grain to grain within a given wire. The amplitude of distribution obviously depends on the Ag/Pd ratio: the higher the silver content, the larger the surface composition distribution. A given $Pd_{100-x}Ag_x$-based array can then be considered as made of more or less distinct wires composed of statistically distributed more or less distinct grains regarding the Ag vs Pd surface composition (Figure 7). Wire to wire behavior toward hydrogen is expected to slightly differ especially regarding the H_2 concentration threshold at which all the gaps within a single wire will close to create a current path. Because a wire has one dimension, it is sufficient that one gap remains open to avoid detection current. There will be wires for which the grain distribution (arrangement along the wire as well as palladium-rich/silver-rich number of grains) will favor gap closing at low concentrations, whereas others will close only at high concentrations of hydrogen. We are claiming these various switch-on concentration thresholds to be at the origin of the correlation between the silver content in $Pd_{100-x}Ag_x$ wires and the corresponding proportional sensitivity window.

CONCLUSION

Hydrogen gas can be detected in the whole concentration range using PdAg mesowire-based sensors with controlled alloy compositions. The lowest hydrogen concentrations can be detected with low silver content alloys but the sensing window is narrowed because of sensor saturation. The sensing window can advantageously be extended to higher hydrogen concentrations for quantitative measurements up to pure H_2 flows with

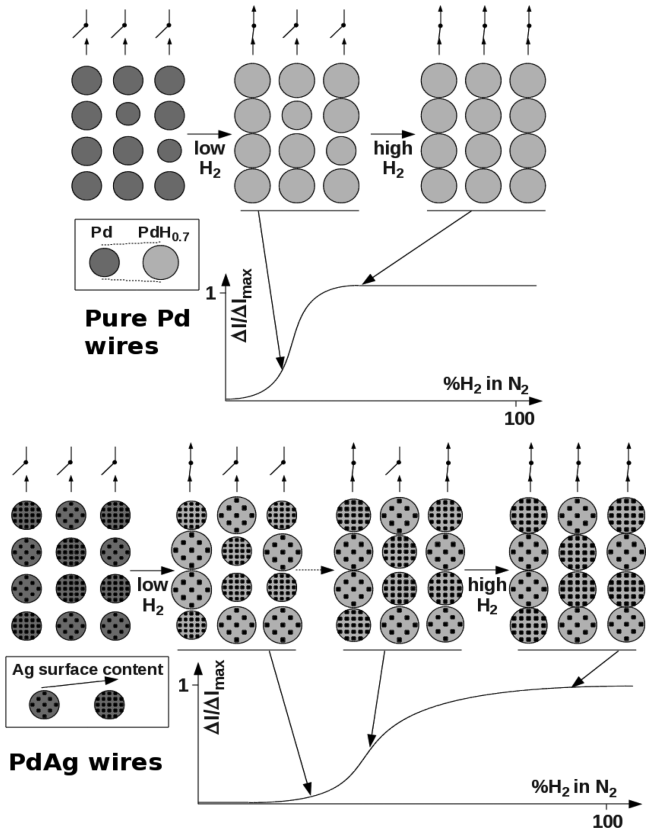

Figure 7. Gap closing mechanism and corresponding normalized current amplitudes (versus H_2 concentration) depending on the wire composition. Pure palladium mesowires (top) tend to "close" in a narrow H_2 concentration range and $\Delta I/\Delta I_{max}$ sigmoid depends on the grain size distribution. Surface composition discrepancies in palladium−silver mesowires (bottom) induce distinct swelling behaviors of grains under H_2 for an expanded $\Delta I/\Delta I_{max}$ sigmoid.

Ag-rich alloys. In contrast, low hydrogen concentrations are inaccessible to these latter sensors. The mechanism responsible for these behaviors implies the statistical distribution in surface composition rather than the structural characteristics and the stability domains of the corresponding hydride phases.

ASSOCIATED CONTENT

Supporting Information

Additional supporting figures and pictures for mesowire synthesis, sensor fabrication, DFT calculations, and in situ XRD as noted in the text. This material is available free of charge via the Internet at http://pubs.acs.org.

AUTHOR INFORMATION

Corresponding Author

*E-mail: fredf@um2.fr.

Notes

The authors declare no competing financial interest.

ACKNOWLEDGMENTS

The authors thank the European community for funding through FP6 Integrated Project HySYS under Project SES6-019981; Dr. Arie Van der Lee, Institut European des Membranes, Montpellier, France for in situ XRD measurements; Pr. Juergen Brugger at LMIS1, EPFL, Lausanne, Switzerland, for providing the metal stencils; Dr. Ouassim

Ghodbane, INRAP, Sidi Thabet, Tunisia; and Dr. Surya Subianto, ICGM, Montpellier, France, for helpful discussions.

REFERENCES

(1) Züttel, A.; Borgschulte, A.; Schlapbach, L. *Hydrogen as a Future Energy Carrier*; Wiley-VCH Verlag GmbH & Co. KGaA: Weinheim, Germany, 2008, *4*, 71−147.
(2) Hübert, T.; Boon-Brett, L.; Black, G.; Banach, U. *Sens. Actuators, B* **2011**, *157*, 329−352.
(3) *Thomson Reuters Web of Knowledge*; http://apps.isiknowledge.com/ (accessed February 4, 2012).
(4) European Patent Office. *Espacenet*; http://worldwide.espacenet.com/ (accessed February 4, 2012).
(5) Lewis, F. A. *The Palladium Hydrogen System*; Academic Press: Londres, 1967; Vol. *XII*, pp 1−178.
(6) Smith, A. L.; Shirazi, H. M. *Thermochim. Acta* **2005**, *432*, 202−211.
(7) Franzier, G. A.; Glosser, R. *J. Phys. D: Appl. Phys.* **1979**, *12*, L113.
(8) Collins, R. L. Hydrogen Detector. U.S. Patent 3 559 457, February 2, 1971; freepatentsonline: 3 559 457.
(9) Zhao, Z.; Sevryugina, Y.; Carpenter, M. A.; Welch, D.; Xia, H. *Anal. Chem.* **2004**, *76* (2), 6321−6326.
(10) Villatoro, J.; Luna-Moreno, D.; Monzon-Hernandez, D. *Sens. Actuators, B* **2005**, *110*, 23−27.
(11) Tobiska, P.; Hugon, O.; Trouillet, A.; Gagnaire, H. *Sens. Actuators, B* **2001**, *74*, 168−172.
(12) Lauf, R. J.; Hoffheins, B. S.; Fleming, P. H. Thin film hydrogen sensor. U.S. Patent 5 367 283, November 22, 1994; freepatentsonline: 5 367 283.
(13) Offermans, P.; Tong, H. D.; van Rijn, C. J. M.; Merken, P.; Brongersma, S. H.; Crego-Calama, M. *Appl. Phys. Lett.* **2009**, *94* (223110), 1−3.
(14) Zeng, X. Q.; Latimer, M. L.; Xiao, Z. L.; Panuganti, S.; Welp, U.; Kwok, W. K.; Xu, T. *Nano Lett.* **2011**, *11*, 262−268.
(15) Im, Y.; Lee, C.; Vasquez, R. P.; Bangar, M. A.; Myung, N. V.; Menke, E. J.; Penner, R. M.; Yun, M. *Small* **2006**, *2*, 356−358.
(16) Wang, M.; Feng, Y. *Sens. Actuators, B* **2007**, *123*, 101−106.
(17) Ji, H.; Wang, X.; Zhao, C.; Zhang, C.; Xu, J.; Zhang, Z. *CrystEngComm* **2011**, *13*, 2617−2628.
(18) DiMeo, F. J.; Chen, B. *Proceedings of the 2000 DOE Program Review*; U.S. Department of Energy: Washington, D.C., 2000.
(19) Zeng, X. Q.; Wang, Y. L.; Deng, H.; Latimer, M. L.; Xiao, Z. L.; Pearson, J.; Xu, T.; Wang, H. H.; Welp, U.; Crabtree, G. W.; Kwok, W. K. *ACS Nano* **2011**, *5*, 7443−7452.
(20) Xie, B.; Liu, L.; Peng, X.; Zhang, Y.; Qian, Xu, Q.; Zheng, M.; Takiya, T.; Han, M. *J. Phys. Chem. C* **2011**, *115*, 16161−16166.
(21) Villanueva, L. G.; Fargier, F.; Kiefer, T.; Ramonda, M.; Brugger, J.; Favier, F. *Nanoscale* **2012**, *4*, 1964−1967.
(22) Graham, T. *Proc. R. Soc. London* **1869**, *17*, 212−220.
(23) Gryaznov, M. *Sep. Purif. Methods* **2000**, *29*, 171−187.
(24) Sonwane, C. G.; Wilcox, J.; Ma, Y. H. *J. Phys. Chem. B* **2006**, *110*, 24549−24558.
(25) Lin, W.-H.; Chang, H.-F. *Surf. Coat. Technol.* **2005**, *194*, 157−166.
(26) Jayaraman, V.; Lin, Y. S. *J. Membr. Sci.* **1995**, *104*, 251−262.
(27) Favier, F.; Walter, E.; Benter, T.; Penner, R. M. *Science* **2001**, 2227−2231.
(28) Walter, E.; Favier, F.; Penner, R. M. *Anal. Chem.* **2002**, *74*, 1546−1553.
(29) Zach, M.; Ng, K.; Penner, R. M. *Science* **2000**, *290*, 2120−2123.
(30) Naidu, S. V. N.; Houska, C. R. *J. Appl. Phys.* **1971**, *42*, 4971−4975.
(31) Xiao, Y.; Weng, B.; Yu, G.; Wang, J.; Hu, B.; Chen, Z. *J. Appl. Electrochem.* **2006**, *36*, 807−812.
(32) Monty, G.; Ng, K. Yang M. Formation of Metal Nanowires for Use as Variable-range Hydrogen Sensors, U.S. Patent 7 237 429, WO2004020978, February 22, 2005; freepatentsonline: 7 237 429.
(33) Osteryoung, R. A.; Kaplan, C.; Hill, D. L. *J. Phys. Chem.* **1961**, *65* (11), 1951−1954.
(34) Bard, A. J.; Parsons, R.; Jordan, J. *Standard Potentials in Aqueous Solution*; Marcel Dekker: New York, 1985, *1*, 1−848.
(35) Fedurco, M.; Kedzierzawski, P.; Augustynski, J. *J. Electrochem. Soc.* **1999**, *146*, 2569−2572.
(36) Murray, B. J.; Walter, E. C.; Penner, R. M. *Nano Lett.* **2004**, *4*, 665−670.
(37) Joska, L.; Marek, M.; Leitner, J. *Biomaterials* **2005**, *26*, 1605−1611.
(38) Tang, L.; Yu, G.; Ouyang, Y.; Si, W.; Weng, B. *Electrochim. Acta* **2008**, *53*, 3305−3312.
(39) Walter, E. C.; Zach, M. P.; Favier, F.; Murray, B. J.; Inazu, K.; Hemminger, J. C.; Penner, R. M. *Chemphyschem* **2003**, *4*, 131−138.
(40) Liu, H.; Favier, F.; Ng, K.; Zach, M. P.; Penner, R. M. *Electrochim. Acta* **2001**, *47*, 671−677.
(41) Lee, J.; Shim, W.; Noh, J.-S.; Lee, W. *ChemPhysChem* **2012**, *13* (6), 1395−1403.
(42) Kiefer, T.; Villanueva, G.; Brugger, J. *Phys. Rev. E* **2009**, *80*, *2* (021104), 1−6.
(43) Kurokawa, H.; Bada, K.; Koyama, M.; Kubo, M.; Miyamoto, A. *Appl. Surf. Sci.* **2005**, *244*, 636−639.
(44) Kim, K. R.; Noh, J. S.; Lee, J. M.; Kim, Y. J.; Lee, W. *J. Mater. Sci.* **2011**, *46*, 1597−1601.
(45) Zeng, X. Q.; Y. L. Wang, Y. L.; Xiao, Z. L.; Latimer, M. L.; T. Xu, T.; Kwok, W. K. *J. Mater. Sci.* **2012**, *47*, 6647−6651.
(46) Mazzolai, F. M.; Paparo, G.; Franco, R. *J. Phys. (Paris)* **1983**, *44* (NC-9), 411−417.